An Image Reconstruction Algorithm for Electrical Impedance Tomography Using Adaptive Group Sparsity Constraint

An Image Reconstruction Algorithm for Electrical Impedance Tomography Using Adaptive Group Sparsity Constraint

Yunjie Yang, *Member, IEEE*, Jiabin Jia*, *Member, IEEE*

***Abstract*— Image quality has long been deemed a key challenge for Electrical Impedance Tomography (EIT). High quality image is of great significance for improving the qualitative and quantitative imaging performance in biomedical or industrial applications. In this paper, a novel image reconstruction algorithm for EIT using adaptive group sparsity constraint is proposed to obtain enhanced image quality. The proposed algorithm takes both the underlying structure characteristics and sparsity prior of the conductivity distribution into account to promote a solution with group sparsity structure and reduce the degree of freedom. Specifically, an adaptive grouping method is incorporated for efficient and dynamic pixel grouping when the conductivity distribution does not have a fixed structure or the prior knowledge of the structure is unavailable. Numerical simulation and phantom experiments are performed to validate the proposed algorithm. The results are compared with those using the Landweber iteration, Total Variation regularization and l_1 regularization. Both simulation and experiment results confirm the significantly improved tomographic imaging quality using the proposed algorithm, which demonstrates great potential for multi-phase flow imaging and biological tissue imaging.**

***Index Terms*— Adaptive group sparsity, Electrical Impedance Tomography, image reconstruction, high quality imaging.**

I. Introduction

ELECTRICAL Impedance Tomography (EIT) is a tomographic imaging modality to non-intrusively reveal the conductivity distribution in either the 2D or 3D sensing domain through boundary current injection and induced voltage measurements [1, 2]. In recent decades, this technique has been extensively exploited in industrial process imaging [3-5] and biomedical imaging [6], owing to its high-speed, non-radiation, and non-intrusive sensing ability. Compared with other tomography modalities, e.g., CT, the application scope of EIT has been promoted by its high temporal resolution, e.g., ~1000 frames per second [1], but limited by the low spatial resolution, e.g., ~10% of the sensor diameter [7]. Aside of the research aspects of advanced instrumentation [1, 8], sensor optimization and sensing strategies [9, 10], the development of image reconstruction algorithms capable of generating high quality tomographic images has especially been deemed a critical challenge for the realization of quantitative and high spatial resolution EIT imaging.

In recent years, a great deal of studies on the EIT image reconstruction problem have been reported in concerned with image quality improvement. A predominant way among them is to identify and then incorporate the known prior knowledge of the conductivity distribution as a constraint term in hope of achieving smaller image error and better spatial resolution. These methods include, for instance, the application of Total Variation regularization with adaptive mesh [11], pre-iterative Landweber [12], high-order differential operator based regularization [13], sparsity regularization [14] and sparsity representation [15] based algorithms, etc. Another prevailing studies based on direct methods, such as the dbar method and Calderon method, were also reported for electrical tomography to obtain the gray value of reconstructed image directly and independently [16-19]. In addition, an open-source Matlab toolkit named EIDORS was developed and has been widely used for three-dimensional EIT image reconstruction problems in the past decades [20], which integrates the most commonly used EIT image reconstruction algorithms. Beyond that, the comprehensive review of the state-of-the-art EIT image reconstruction algorithms is also well summarized and thoroughly discussed in [21] and [22]. In spite of existing achievements, it is still highly requisite to develop EIT image reconstruction algorithms with higher spatial resolution and smaller image error for the purpose of high definition conductivity imaging.

In this paper, we propose a novel image reconstruction algorithm for EIT using an adaptive group sparsity constraint to achieve high quality conductivity imaging. The concept of sparsity gains popularity since last decade with the maturity of compressive sensing theory [23], which has been extensively investigated and applied in signal processing, image processing and solve of inverse problems such as image reconstruction problems of electrical-based tomography [14, 15]. Under some circumstances, the conductivity distribution of the sensing object is naturally sparse or sparse under certain basis, which can be regarded as prior knowledge and exploited to promote nonzero coefficients while suppresses the noise close to zeroes. As an extension of the conventional sparsity concept, the idea of group sparsity was further proposed recently to incorporate with the underlying structure of the solutions on the basis of the

Manuscript received xx, xx, 2016. This work was partially supported by the 2015 IEEE I&M Society Graduate Fellowship Award.

Yunjie Yang and Jiabin Jia* are with the Agile Tomography Group, Institute for Digital Communications, School of Engineering, The University of Edinburgh, Edinburgh, EH9 3JL, UK (e-mail: jiabin.jia@ed.ac.uk).

sparse priors [24]. In this work, the group sparsity prior is investigated for high quality EIT imaging. An adaptive grouping method is proposed for efficient and dynamic pixel grouping for the case that the structure of target conductivity distribution is not fixed or the prior knowledge of the structure is unavailable. On this basis, an adaptive group sparsity constrained algorithm (AGSP) for EIT is further developed to improve spatial resolution and reduce image error. Compared with the reported algorithms [11-15, 21, 22], the novelty of AGSP includes: a) adaptively encoding of the structure characteristics of conductivity variation as prior information; b) integration of sparsity constraint on the group structures for superior noise reduction performance. The AGSP algorithm is comprehensively evaluated by numerical simulation study and phantom experiments. The performance is quantitatively compared with conventional iterative algorithms. Attributing to its enhanced spatial resolution and superior noise reduction performance, the AGSP algorithm can be potentially applied in the areas with relatively high requirement on spatial resolution and noise performance, for example, dispersed phase imaging in multi-phase flow applications [25], cancer cell spheroid imaging during cell culture process and tissue culture monitoring in biomedical applications [26].

The structure of the paper is organized as follows: Section II describes the principle of EIT. Section III demonstrates the AGSP algorithm. Section IV gives the numerical simulation and phantom experiment results. Finally, Section V illustrates the concluding remarks and discusses the future work.

II. Electrical Impedance Tomography

As shown in Fig. 1, given a bounded, simple connected domain $\Omega \in R^d$, $d \geq 2$, EIT is to estimate the conductivity distribution in Ω by successively injecting a pair of complementary alternating current, i.e., $[I_e, -I_e]$ into the selected electrodes and measuring the induced boundary voltage, i.e., $[V_a, V_b]$ across another pair of electrodes. The relationship between conductivity distribution in the sensing domain and induced boundary voltage is expressed as

$$\mathbf{V}=\mathrm{F}(\boldsymbol{\sigma})+\mathbf{e} \tag{1}$$

where F is the nonlinear forward operator and $\mathbf{e}$ is noise; $\boldsymbol{\sigma}$ is the conductivity distribution in Ω. Eq. (1) can be linearized and the approximate relationship between conductivity variation $\Delta\boldsymbol{\sigma}$ and induced voltage change $\Delta\mathbf{V}$ can be formulated as

$$\Delta\mathbf{V}=\mathbf{J}\Delta\boldsymbol{\sigma} \tag{2}$$

where $\mathbf{J}$ is the Jacobian matrix which is calculated by

$$\mathbf{J}_{cm}(x,y)=\frac{\partial V_{cm}}{\partial \sigma_k}=-\int_{\text{pixel }k}\nabla\mathbf{u}(I^c)\cdot\nabla\mathbf{u}(I^m)\,dV \tag{3}$$

where $\mathbf{J}_{cm}(x, y)$ is the sensitivity at pixel (x, y) when the electrode pairs c and m are set as current injection and measurement electrodes, respectively; $\mathbf{u}(I^c)$ and $\mathbf{u}(I^m)$ denote the electrical potential distribution in Ω when the c^{th} and m^{th} electrode pairs are selected as current injection, respectively.

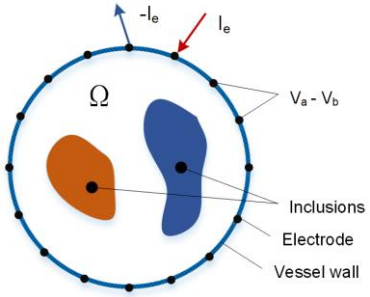

Fig. 1. Schematic illustration of EIT sensing principle.

Generally, based on Eq. (2), the conductivity variation in Ω can be estimated by solving the following constrained optimization problem:

$$\begin{cases}\min\limits_{\Delta\boldsymbol{\sigma}} & \mathrm{R}(\Delta\boldsymbol{\sigma}) \\ s.t. & \mathbf{J}\Delta\boldsymbol{\sigma}=\Delta\mathbf{V}\end{cases} \tag{4}$$

where R is the regularization function, which incorporates a particular prior knowledge of the conductivity variation.

III. Adaptive Group Sparsity Constrained Method

A. Conventional Landweber Iteration, L_1 Regularization and Total Variation Regularization Methods

The subsection briefly introduces three prevailing iterative EIT image reconstruction algorithms which will be used as comparing algorithms in the following sections.

The first method is Landweber iteration [27]. The updating form of Landweber iteration for EIT is expressed by

$$\Delta\boldsymbol{\sigma}^{i+1}=\Delta\boldsymbol{\sigma}^{i}-\alpha\mathbf{J}^{\mathrm{T}}(\Delta\mathbf{V}-\mathbf{J}\Delta\boldsymbol{\sigma}^{i}) \tag{5}$$

where α is the step factor of each iteration.

The second method is l_1 regularization (or sparsity regularization) [15]. l_1 regularization is effective for imposing sparsity constraint on conductivity variation. The EIT image reconstruction based on l_1 regularization can be formulated as

$$\begin{cases}\min\limits_{\mathbf{a}} & \|\mathbf{a}\|_1 \\ s.t. & \mathbf{J}\boldsymbol{\Phi}\mathbf{a}=\Delta\mathbf{V}\end{cases} \tag{6}$$

where $\Delta\boldsymbol{\sigma}=\boldsymbol{\Phi}\mathbf{a}$; $\mathbf{a}$ is the sparse coefficient vector of the conductivity variation distribution under certain basis, for instance, a wavelet basis or a learned dictionary. Specifically, $\boldsymbol{\Phi}$ equaling identity matrix indicates the conductivity variation distribution is naturally sparse, and in this case $\Delta\boldsymbol{\sigma}=\mathbf{a}$. The l_1 norm of the coefficient vector, i.e., $\|\mathbf{a}\|_1$, is then minimized for sparse recovery. Eq. (6) facilitates the recovery of a high dimensional signal with a much smaller number of measurements. In this work, the method reported by Ewout et al. [28] is adopted to solve Eq. (6).

Another iterative algorithm widely applied in EIT is Total Variation (TV) regularization [29]. TV regularization is

particularly effective for estimating the conductivity variation distribution with a sharp boundary. The method can be formulated as

$$\begin{cases} \min\limits_{\Delta\boldsymbol{\sigma}} & \|\Delta\boldsymbol{\sigma}\|_{\mathrm{TV}} \\ s.t. & \mathbf{J}\Delta\boldsymbol{\sigma}=\Delta\mathbf{V} \end{cases} \tag{7}$$

where $\|\Delta\boldsymbol{\sigma}\|_{\mathrm{TV}}$ is the TV norm of the conductivity variation distribution, which equals to the l_1 norm of the gradient of the conductivity variation distribution, as defined by

$$\begin{aligned} \|\Delta\boldsymbol{\sigma}\|_{\mathrm{TV}} &= \sum_{x,y}\sqrt{(\mathrm{D}^{v}_{x,y}(\Delta\boldsymbol{\sigma}))^2+(\mathrm{D}^{h}_{x,y}(\Delta\boldsymbol{\sigma}))^2} \\ &= \sum_{x,y}\left|\nabla_{x,y}(\Delta\boldsymbol{\sigma})\right| \\ &= \|\nabla(\Delta\boldsymbol{\sigma})\|_1 \end{aligned} \tag{8}$$

where (x, y) is the coordinate of a pixel in Ω. $\mathrm{D}^{v}_{x,y}(\Delta\boldsymbol{\sigma})$ and $\mathrm{D}^{h}_{x,y}(\Delta\boldsymbol{\sigma})$ are the derivatives of $\Delta\boldsymbol{\sigma}$ along the vertical and horizontal direction, respectively, and can be expressed as

$$D^{h}_{x,y}(\Delta\boldsymbol{\sigma})=\begin{cases}\Delta\boldsymbol{\sigma}_{x,y}-\Delta\boldsymbol{\sigma}_{x+1,y} & 1\le x<P\\ 0 & x=P\end{cases} \tag{9}$$

$$D^{v}_{x,y}(\Delta\boldsymbol{\sigma})=\begin{cases}\Delta\boldsymbol{\sigma}_{x,y}-\Delta\boldsymbol{\sigma}_{x,y+1} & 1\le y<P\\ 0 & y=P\end{cases} \tag{10}$$

where, P is the number of pixels in each direction. As indicated by Eq. (8), TV regularization can be regarded as a particular form of sparsity regularization, which promotes a solution with sparse image gradient. In this work, Eq. (7) is solved by the gradient-based recovery method [30, 31], whose iteration form is given by

$$\Delta\boldsymbol{\sigma}^{i+1}_{x,y}=\Delta\boldsymbol{\sigma}^{i}_{x,y}-\alpha\left\{\nabla_{x,y}\left(\frac{1}{2}\left\|\Delta\mathbf{V}-\mathbf{J}\Delta\boldsymbol{\sigma}^{i}\right\|_2^2\right)+\nabla_{x,y}\left(\left\|\Delta\boldsymbol{\sigma}^{i}\right\|_{\mathrm{TV}}\right)\right\} \tag{11}$$

where α is the iteration step size of the i^{th} iteration. The gradient of TV norm is calculated using a smooth approximation strategy to avoid a zero denominator, which is expressed as

$$\begin{aligned}\nabla_{x,y}\left(\|\Delta\boldsymbol{\sigma}\|_{\mathrm{TV}}\right)=&\frac{D^{h}_{x,y}(\Delta\boldsymbol{\sigma})+D^{v}_{x,y}(\Delta\boldsymbol{\sigma})}{\sqrt{(\mathrm{D}^{v}_{x,y}(\Delta\boldsymbol{\sigma}))^2+(\mathrm{D}^{h}_{x,y}(\Delta\boldsymbol{\sigma}))^2+\varepsilon}}-\\ &\frac{D^{h}_{x-1,y}(\Delta\boldsymbol{\sigma})}{\sqrt{(\mathrm{D}^{v}_{x-1,y}(\Delta\boldsymbol{\sigma}))^2+(\mathrm{D}^{h}_{x-1,y}(\Delta\boldsymbol{\sigma}))^2+\varepsilon}}-\\ &\frac{D^{v}_{x,y-1}(\Delta\boldsymbol{\sigma})}{\sqrt{(\mathrm{D}^{v}_{x,y-1}(\Delta\boldsymbol{\sigma}))^2+(\mathrm{D}^{h}_{x,y-1}(\Delta\boldsymbol{\sigma}))^2+\varepsilon}}\end{aligned} \tag{12}$$

where ε is the relaxation parameter, which is 1e-7 in this work.

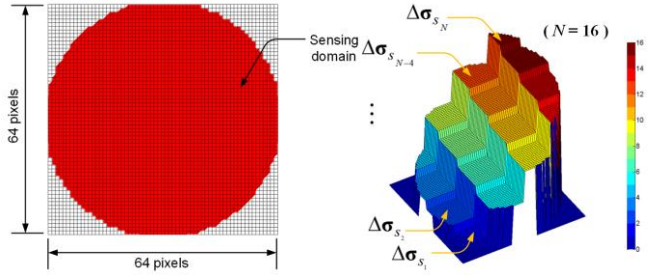

(a) (b)

Fig. 2. Schematic illustration of pixel grouping. (a) The mesh for image reconstruction. (b) A grouping example with 16 quadrate shape groups.

B. The Proposed AGSP Algorithm

Conventional sparsity regularization methods demonstrated in the last subsection make use of only the sparsity of conductivity variation distribution as prior knowledge, i.e., either the conductivity variation itself or its transform under certain basis or its gradient is sparse. To further improve the image recoverability, this work takes advantage of additional information about the underlying structure of the conductivity variation, which extends the scope of sparsity. In majority of EIT applications, the conductivity variation distributions contain group sparsity structure. Namely, the conductivity change with respect to the background substance naturally groups together rather than randomly distributes in the sensing domain. On this occasion, the combined constraint of sparsity and structure characteristics can be applied to reduce the degree of freedom and improve the recoverability.

Fig. 2(a) illustrates the pixel mesh for solving the EIT image reconstruction problem in this work. The sensing domain is discretized into 64 ×64 pixels and 3228 pixels are in the circular area. To implement the combined constraint of sparsity and structure characteristics, the discretized pixels within the sensing domain should be grouped according to conductivity variation. An intuitive pixel-grouping example with fixed quadrate shape and total group number N=16 is shown in Fig. 2(b) (note here in practical cases, more complicated grouping will be adopted based on the conductivity variation). Given that the conductivity variation vector $\Delta\boldsymbol{\sigma}$ can be divided into N disjoint groups $\{\Delta\boldsymbol{\sigma}_{S_1},\Delta\boldsymbol{\sigma}_{S_2},...,\Delta\boldsymbol{\sigma}_{S_N}\}$ and $\mathrm{U}_{i=1}^{N}\Delta\boldsymbol{\sigma}_{S_i}=\Delta\boldsymbol{\sigma}$ which guarantees the complete cover, then to incorporate group sparsity prior, the EIT image reconstruction problem depicted by Eq. (4) can be formulated using the weighted group-sparse basis pursuit model with non-negative constraint as expressed below

$$\begin{cases}\min\limits_{\Delta\boldsymbol{\sigma}} & \|\Delta\boldsymbol{\sigma}\|_{w,2,1}:=\sum\limits_{i=1}^{N}w_i\left\|\Delta\boldsymbol{\sigma}_{S_i}\right\|_2\\ s.t. & \mathbf{J}\Delta\boldsymbol{\sigma}=\Delta\mathbf{V},\\ & g(\Delta\boldsymbol{\sigma})\cdot\Delta\boldsymbol{\sigma}\ge 0\end{cases} \tag{13}$$

where $\|\Delta\boldsymbol{\sigma}\|_{w,2,1}$ is the weighted $l_{2,1}$ norm, which is proved to promote the group sparsity and generate a convex problem [24, 32]; N is the number of groups and S_i is the group index of the i^{th}

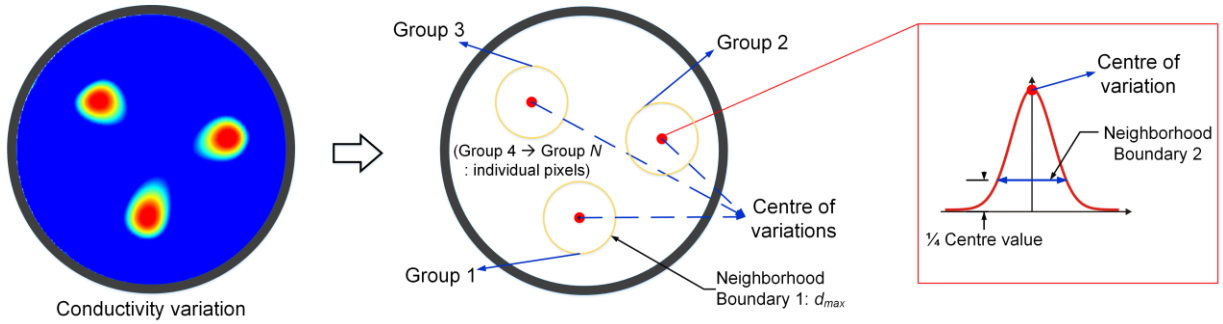

Fig. 3. Schematic illustration of the adaptive grouping idea.

group. w_i is the weight for the i^{th} group. To further improve the noise reduction performance, the non-negative constraint is applied on the dot multiplication $g(\Delta\boldsymbol{\sigma})\cdot\Delta\boldsymbol{\sigma}$, where the operator g is defined by

$$g(\Delta\boldsymbol{\sigma}) = [sign(sum(\Delta\boldsymbol{\sigma}_{S_1}))\cdot\mathbf{H}_{S_1}, ...sign(sum(\Delta\boldsymbol{\sigma}_{S_i}))\cdot\mathbf{H}_{S_i}, ...]^{\mathrm{T}} \tag{14}$$

where *sign* denotes the sign function; *sum* denotes the summation of a vector; $\mathbf{H}_{S_i} = [1, 1, \ldots, 1]$ is the all one vector with the same length of the pixel numbers within the i^{th} group S_i.

A key challenge of implementing the proposed algorithm depicted in Eq. (13) is prompt and reasonable grouping of the conductivity variation based on the measurement, especially when there is no prior information available to predict the structure of conductivity variation. In this work, an adaptive grouping method is proposed to incorporate with Eq. (13) to tackle this problem. The basic idea is to group together the pixels with similar conductivity variation within a reasonable neighborhood of each inclusion. Fig. 3 shows the schematic illustration of the adaptive grouping method. First of all, the conductivity variation is estimated by the one-step Gaussian Newton solver with Laplacian regularization [13], which is expressed as

$$\Delta\hat{\boldsymbol{\sigma}} = (\mathbf{J}^{\mathrm{T}}\mathbf{J} + \lambda\mathbf{L}^{\mathrm{T}}\mathbf{L})^{-1}\mathbf{J}^{\mathrm{T}}\Delta\mathbf{V} \tag{15}$$

where λ is the regularization factor. L is the four-connected region second order Laplacian operator matrix [13]. There are two reasons to adopt this method in our work: 1) the estimation generated from the method is good enough for grouping; 2) this method has a low computation cost which facilitates the real-time performance.

After obtaining the estimation, the center of variations can be identified by calculating the local maximum points, as the red points shown in the middle of Fig. 3. Then several large groups around each center can be formed while the remaining part generates a number of small groups per individual pixel. As a result, the idea will form a number of large groups based on the number of inclusions, whilst other individual pixels will not be grouped but counted as a small group. Regarding the large groups, two criteria are applied to determine the boundary of each group, which are depicted as following:

a) *Criterion 1*: The first criterion empirically illustrates the boundary of the neighborhood of each inclusion, i.e., boundary 1 as shown in the middle of Fig. 3. It determines the outermost border of each large group, which includes the pixels within a reasonable geometrical region. This is to avoid the situation that two pixels with a large distance are grouped together. Boundary 1 is calculated by the maximum diameter d_{max} as the yellow circles shown in the middle part of Fig. 3. The value of d_{max} is selected empirically according to specific applications, and in this work, d_{max} is set as 20 pixels.

b) *Criterion 2*: The second criterion provides a finer boundary of each group inside the outermost border defined by the first criterion, i.e., boundary 2 as shown in the right part of Fig. 3. Boundary 2 is determined by the pixels with a conductivity variation equal to a quarter of the conductivity variation at the center of each inclusion, as shown in the red box on the right of Fig. 3. That is, the pixels with a conductivity variation larger

TABLE I
ADAPTIVE GROUP SPARSITY CONSTRAINED ALGORITHM

Algorithm: Adaptive group sparsity constrained algorithm (AGSP)

Input: The measured voltage vector $\Delta\mathbf{V}$, the maximum group diameter d_{max}, and the weight vector $\mathbf{w}$

Step 1: Estimate the conductivity variation distribution by the one-step Gaussian Newton solver with Laplacian regularization shown in Eq. (15).

Step 2: Based on the estimated result $\Delta\hat{\boldsymbol{\sigma}}$, calculate the mean $|\Delta\hat{\boldsymbol{\sigma}}|_{mean}$ and the standard deviation $|\Delta\hat{\boldsymbol{\sigma}}|_{std}$ of its absolute value $|\Delta\hat{\boldsymbol{\sigma}}|$.

Step 3: Apply the filter defined as following:

$$\begin{cases} |\Delta\hat{\boldsymbol{\sigma}}|_i = |\Delta\hat{\boldsymbol{\sigma}}|_i, & if\ |\Delta\hat{\boldsymbol{\sigma}}|_i > |\Delta\hat{\boldsymbol{\sigma}}|_{mean} + |\Delta\hat{\boldsymbol{\sigma}}|_{std} \\ |\Delta\hat{\boldsymbol{\sigma}}|_i = 0, & if\ |\Delta\hat{\boldsymbol{\sigma}}|_i \le |\Delta\hat{\boldsymbol{\sigma}}|_{mean} + |\Delta\hat{\boldsymbol{\sigma}}|_{std} \end{cases}, i = 1, \ldots, 3228$$

Step 4: Calculate index vector **D** of all local maximum points of $|\Delta\hat{\boldsymbol{\sigma}}|$.

Step 5: Calculate the group index vector **G**:

for i=1: *number of local maximum points* **do**
  for j=1:*total pixel number* **do**
    if $|\Delta\hat{\boldsymbol{\sigma}}|_j > \frac{1}{4}|\Delta\hat{\boldsymbol{\sigma}}|_{\mathbf{D}(i)}$ and $\|\mathbf{C}_j - \mathbf{C}_{\mathbf{D}(i)}\|^2 < (\frac{d_{\max}}{2})^2$
      G(j)=i

(**C** is the coordinate vector of pixels)

k=1

for $t \in$ all other elements in **G** **do**
  G(t(k))= *number of local maximum points*+k
  k=k+1

Step 6: Solve the group-sparse basis pursuit model illustrated in Eq. (13).

Output: The final estimated conductivity variation distribution.

than a quarter of the maximum value at the center of each inclusion are regarded to be within boundary 2.

The final pixel grouping set is calculated as the intersection of the two regions within boundary 1 and boundary 2. As the grouping result is calculated based on the one-step estimation, it may change slightly when the signal to noise ratio (SNR) of the voltage measurement becomes lower. However, the proposed AGSP does not require a precise estimation of the inclusion boundary, instead it only requires the inclusion is completely contained in the group. Therefore, with a reasonable SNR such as 50 dB or higher (which can be achieved by most of reported EIT systems), criterion 2 can generate a stable enough boundary of a group. Through the proposed method, the pixel groups associated with conductivity variation can be adaptively calculated and the group sparse prior can be effectively integrated into Eq. (13). Finally, the EIT image reconstruction problem is solved by using the modified group-sparse basis pursuit model illustrated in Eq. (13). The overall algorithm is named as adaptive group sparsity constrained algorithm (AGSP). The detail implementation of AGSP is illustrated in TABLE I.

In TABLE I, the adaptive pixel grouping result is firstly calculated through Step 1 to Step 5. The grouping result is illustrated by a group index vector **G** whose length is the same as the total number of pixels. In Step 2, the absolute value of the estimated conductivity variation from Step 1 is adopted in order to deal with the situation with either positive or negative or bi-direction conductivity changes. Then in Step 3, the absolute conductivity variance is filtered using a threshold defined by the summary of its mean and standard deviation. The filter is to eliminate the noise that may affect the calculation of local maximum points in Step 4. Furthermore, all of the local maximum points which demotes the centers of large groups are identified. While in Step 5, pixels belong to the same large group are identified by the aforementioned two criteria and given the same group index value in **G**. At the end, in Step 6, the grouping index vector **G** denoting the pixel grouping result is integrated with Eq. (13) to iteratively estimate the conductivity variation.

To solve Eq. (13), the alternating direction method of multipliers (ADMM) can be adopted [32, 33]. ADMM is a method to solve convex optimization problems by breaking them into easier sub-problems [32]. ADMM solves the optimization problem with the following form:

$$\begin{cases} \min\limits_{\mathbf{x},\,\mathbf{z}} & f(\mathbf{x}) + h(\mathbf{z}) \\ s.t. & \mathbf{A}\mathbf{x} + \mathbf{B}\mathbf{z} = \mathbf{E} \end{cases} \tag{16}$$

By introducing an auxiliary variable **z**, Eq. (13) can be firstly rewritten as the following equivalent form

$$\begin{cases} \min\limits_{\Delta\boldsymbol{\sigma},\,\mathbf{z}} & \|\mathbf{z}\|_{w,2,1} := \sum\limits_{i=1}^{N} w_i \left\|\mathbf{z}_{s_i}\right\|_2 \\ s.t. & \mathbf{z} = \Delta\boldsymbol{\sigma},\ \mathbf{J}\Delta\boldsymbol{\sigma} = \Delta\mathbf{V}, \\ & g(\Delta\boldsymbol{\sigma}) \cdot \Delta\boldsymbol{\sigma} \geq 0 \end{cases} \tag{17}$$

TABLE II
ADMM FOR THE MINIMIZATION PROBLEM IN EQ. (18)

Initialization: Starting point ($\mathbf{z}$, $\Delta\boldsymbol{\sigma}$, $\boldsymbol{\mu}_1$, $\boldsymbol{\mu}_2$, η_1, η_2, α_1, α_2)

iteration:

a) solve the $\Delta\boldsymbol{\sigma}$-subproblem:

$$\Delta\boldsymbol{\sigma}_{k+1} = \arg\min_{\Delta\boldsymbol{\sigma}} \ \boldsymbol{\mu}_1^{\mathrm{T}}\Delta\boldsymbol{\sigma}_k + \frac{\eta_1}{2}\|\mathbf{z} - \Delta\boldsymbol{\sigma}_k\|_2^2 - \ldots \boldsymbol{\mu}_2^{\mathrm{T}}\mathbf{J}\Delta\boldsymbol{\sigma}_k + \frac{\eta_2}{2}\|\mathbf{J}\Delta\boldsymbol{\sigma}_k - \Delta\mathbf{V}\|_2^2$$

b) solve the z-subproblem:

$$\mathbf{z}_{k+1} = \arg\min_{\mathbf{z}} \ \sum_{i=1}^{N} w_i \left\|\mathbf{z}_{s_i}\right\|_2 - \boldsymbol{\mu}_1^{\mathrm{T}}\mathbf{z} + \frac{\eta_1}{2}\|\mathbf{z} - \Delta\boldsymbol{\sigma}\|_2^2$$

c) update the multipliers:

$$\boldsymbol{\mu}_1 = \boldsymbol{\mu}_1 - \alpha_1\eta_1(\mathbf{z} - \Delta\boldsymbol{\sigma})$$

$$\boldsymbol{\mu}_2 = \boldsymbol{\mu}_2 - \alpha_2\eta_2(\mathbf{J}\Delta\boldsymbol{\sigma} - \Delta\mathbf{V})$$

until a stopping criterion is satisfied.

where Eq. (17) can be further rewritten using the augmented Lagrangian problem form as an unconstrained form:

$$\min_{\Delta\boldsymbol{\sigma},\,\mathbf{z}} \ \sum_{i=1}^{N} w_i \left\|\mathbf{z}_{s_i}\right\|_2 - \boldsymbol{\mu}_1^{\mathrm{T}}(\mathbf{z} - \Delta\boldsymbol{\sigma}) + \frac{\eta_1}{2}\|\mathbf{z} - \Delta\boldsymbol{\sigma}\|_2^2 - \ldots \boldsymbol{\mu}_2^{\mathrm{T}}(\mathbf{J}\Delta\boldsymbol{\sigma} - \Delta\mathbf{V}) + \frac{\eta_2}{2}\|\mathbf{J}\Delta\boldsymbol{\sigma} - \Delta\mathbf{V}\|_2^2 \tag{18}$$

where $\boldsymbol{\mu}_1$ and $\boldsymbol{\mu}_2$ are multipliers and η_1 and η_2 are penalty parameters. Eq. (18) has been proved to converge to the solution of Eq. (17) [32] and is tackled using the algorithm illustrated in TABLE II. By applying ADMM, Eq. (18) is broken into the $\Delta\boldsymbol{\sigma}$-subproblem and the **z**-subproblem. The $\Delta\boldsymbol{\sigma}$-subproblem is a convex quadratic problem which can be directly solved in one step while the **z**-subproblem can be rewritten as

$$\begin{aligned} \mathbf{z}_{k+1} &= \arg\min_{\mathbf{z}} \ \sum_{i=1}^{N} \left(w_i \left\|\mathbf{z}_{s_i}\right\|_2 - \boldsymbol{\mu}_1^{\mathrm{T}}\mathbf{z}_{s_i} + \frac{\eta_1}{2}\|\mathbf{z}_{s_i} - \Delta\boldsymbol{\sigma}_{s_i}\|_2^2\right) \\ &= \arg\min_{\mathbf{z}} \ \sum_{i=1}^{N} \left(w_i \left\|\mathbf{z}_{s_i}\right\|_2 + \frac{\eta_1}{2}\|\mathbf{z}_{s_i} - \Delta\boldsymbol{\sigma}_{s_i} - \frac{1}{\eta_1}\boldsymbol{\mu}_{s_i}\|_2^2 + \mathrm{M}(\Delta\boldsymbol{\sigma}_{s_i})\right) \end{aligned} \tag{19}$$

where $\mathrm{M}(\Delta\boldsymbol{\sigma}_{s_i})$ is a function of $\Delta\boldsymbol{\sigma}_{s_i}$ which has no effect on the result therefore can be taken as a constant in the **z**-subproblem. Eq. (19) has a closed form solution by applying the group-wise soft thresholding [33]. Note that the non-negative constraint $g(\Delta\boldsymbol{\sigma})\cdot\Delta\boldsymbol{\sigma} \geq \mathbf{0}$ is applied during each iteration.

For the proposed AGSP, appropriate weight w_i chosen based on prior knowledge may improve recovery performance, and for the simplest case, w_i=1 can be applied to treat each group equally. Moreover, a smaller weight can be given to the large groups compared with other small groups to promote the sparsity of the estimation for large groups. For instance, the weight can be calculated by

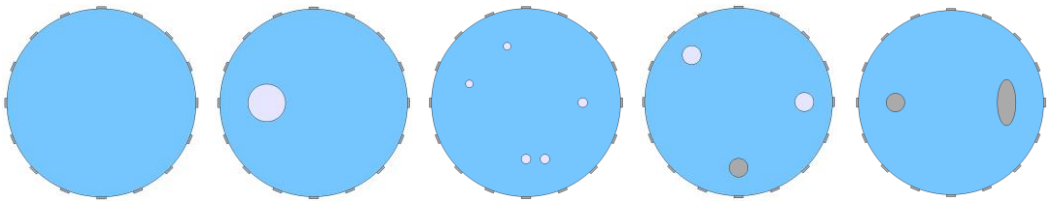

(a) (b) (c) (d) (e)

Fig. 4. The modelled EIT sensor and simulation phantoms. (a) The 16-electrode EIT sensor. (b) Phantom 1. (c) Phantom 2. (d) Phantom 3. (e) Phantom 4.

$$\begin{cases} w_i = \dfrac{1}{N_b + 2N_s} & \text{if the } i^{th} \text{ group is large,} \\ w_i = \dfrac{2}{N_b + 2N_s} & \text{if the } i^{th} \text{ group is small,} \\ N_b + N_s = N \end{cases} \tag{20}$$

where N_b is the number of large groups and N_s is the number of small groups; N is the total number of groups. Eq. (20) shows a weighting example that the weight of large group is half of that of the small group under the assumption that $\sum_{i=1}^{N} w_i = 1$. The influence of weight on image quality is further discussed in Section IV.

In summary, several remarks of the proposed AGSP method are as following:

1) A group index vector with the same length as the total pixel number is defined to denote the adaptive grouping result.
2) Pixels within the same group have the same group index value.
3) The group contains more than one pixel is defined as a large group in the following context.
4) The group contains only one pixel is defined as a small group in the following context.
5) The groups may overlap.
6) The grouping method guarantees complete cover.

IV. Results and Discussion

The proposed AGSP is comprehensively evaluated in this section by numerical simulation and a series of phantom experiments. The performance of AGSP is compared with that of the conventional Landweber iteration (Eq. (5)), l_1 regularization (Eq. (6)), and TV regularization algorithm (Eq. (7)), which are popularly applied in image reconstruction and denoise problems.

A. Numerical Simulation

As illustrated in Fig. 4(a), a 16-electrode EIT sensor is modelled in COMSOL Multiphysics for numerical evaluation of the proposed AGSP algorithm. The diameter of the sensor is 95 mm. The background substance is saline with a conductivity value of 0.05 S · m^{-1}. Four conductivity variation phantoms, i.e., phantom 1 to phantom 4, are established, as shown from Fig. 4(b) to Fig. 4(e) respectively. Phantom 1 simulates a large air bubble (non-conductive) with an object-sensor diameter ratio of 20%. Phantom 2 simulates five dispersed small air bubbles with two different object-sensor diameter ratios, i.e., 4% (left top bubbles) and 5% (right below bubbles). Phantom 3 simulates three objects with an object-sensor diameter ratio of 10% and different conductivities, i.e., 0.03 S · m^{-1} of the left object, 0.01 S · m^{-1} of the right object and 1e+7 S · m^{-1} of the bottom object. Phantom 4 simulates two conductive objects (1e+7 S · m^{-1}) with an object-sensor diameter ratio larger than 10% and different shapes.

In simulation, to obtain the boundary voltage data, the adjacent sensing strategy is applied and a data frame is composed of 104 measurements [34]. All the measurement data contain white noise with 50 dB SNR. When implementing the Landweber iteration, l_1 regularization, TV regularization and the proposed AGSP algorithm, the maximum iteration number is set as 500 and the stopping tolerance is select to be 1e-7. The iteration will stop if either condition is firstly met. The algorithm parameters, such as step factors and weights are empirically determined based on a series of practices and the same parameters are applied to the test phantoms, as illustrated in the first row of TABLE III.

To quantitatively evaluate the accuracy of the reconstructed images, the relative image error (*IE*) and correlation coefficient (*CC*) between the normalized conductivity variation and the true phantom are employed. The definition of *IE* and *CC* is expressed as

$$IE = \frac{\left\| \Delta\boldsymbol{\sigma} - \Delta\boldsymbol{\sigma}_{true} \right\|}{\left\| \Delta\boldsymbol{\sigma}_{true} \right\|} \tag{21}$$

$$CC = \frac{\sum_{i=1}^{p} \left(\Delta\boldsymbol{\sigma}_i - \Delta\boldsymbol{\sigma}_{avr} \right) \left(\Delta\boldsymbol{\sigma}_{true,\,i} - \Delta\boldsymbol{\sigma}_{true,\,avr} \right)}{\sqrt{\sum_{i=1}^{p} \left(\Delta\boldsymbol{\sigma}_i - \Delta\boldsymbol{\sigma}_{avr} \right)^2 \sum_{i=1}^{p} \left(\Delta\boldsymbol{\sigma}_{true,\,i} - \Delta\boldsymbol{\sigma}_{true,\,avr} \right)^2}} \tag{22}$$

where $\Delta\boldsymbol{\sigma}$ and $\Delta\boldsymbol{\sigma}_{true}$ are the reconstructed conductivity variation and true conductivity variation, respectively; p is the number of pixels and in this work p=3228; $\Delta\boldsymbol{\sigma}_i$ and $\Delta\boldsymbol{\sigma}_{avr}$ are the i^{th} element and the average of the reconstructed conductivity variation, respectively; $\Delta\boldsymbol{\sigma}_{true,i}$ and $\Delta\boldsymbol{\sigma}_{true,avr}$ are the i^{th} element and the average of the true conductivity variation, respectively.

TABLE III illustrates the image reconstruction results, relative image error and correlation coefficient based on the Landweber iteration, TV regularization, l_1 regularization and the proposed AGSP algorithm. The pixel grouping result of each phantom is shown in TABLE IV, where the large groups are highlighted using different colors while the small groups are depicted with the same light green color. Phantom 1 is designed to evaluate the reconstruction performance of large objects. The ratio of the object and sensor diameter is 20%. Compared with

TABLE III
IMAGE RECONSTRUCTION RESULTS BASED ON NOISY SIMULATION DATA (SNR=50 DB)

Phantom	**Landweber** Step factor α in Eq.(5): 2	**L_1** Step factor solving Eq. (6): 2	**TV** Step factor α in Eq. (11): 2	**AGSP** d_{max}: 20; **w**: Eq. (20), λ: 0.01
	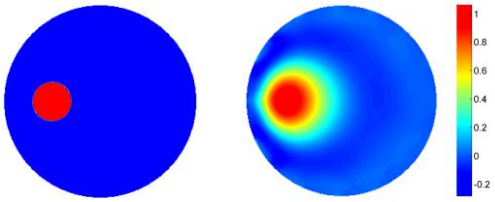	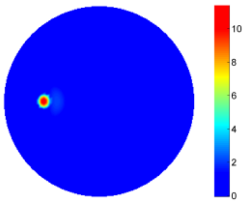	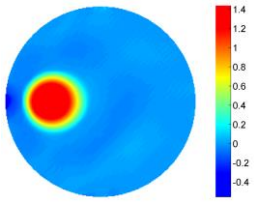	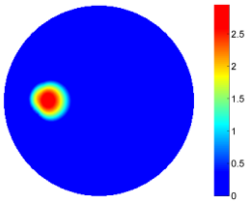
IE [%]	87.87	85.64	64.13	47.47
CC	0.6840	0.6238	0.8212	0.9192
	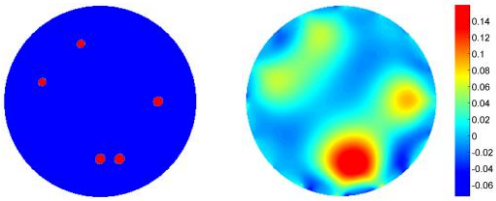	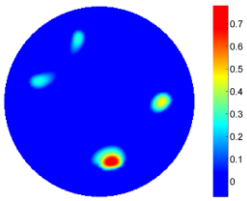	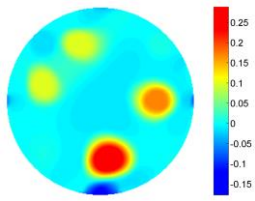	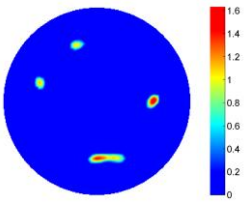
IE [%]	244.6	100.1	202.8	64.88
CC	0.2374	0.4567	0.3108	0.7621
	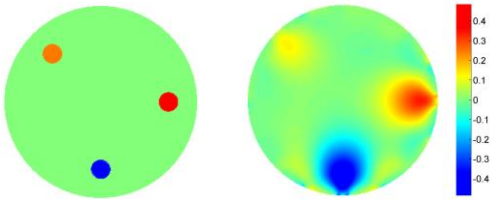	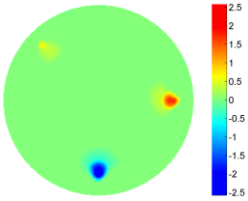	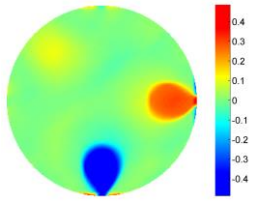	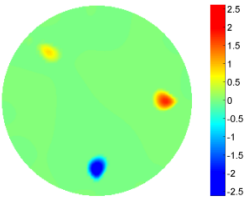
IE [%]	177.6	61.16	154.7	42.21
CC	0.4769	0.7940	0.4562	0.9098
	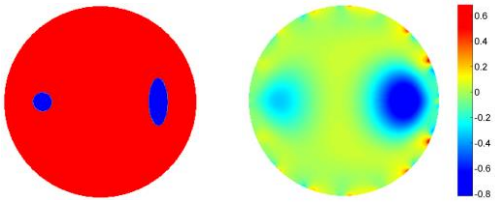	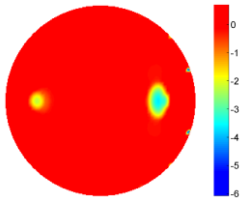	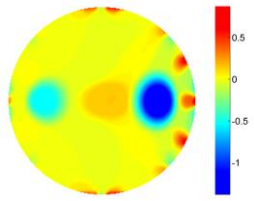	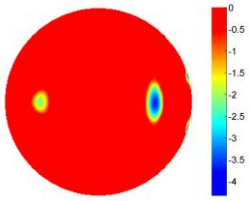
IE [%]	126.4	97.70	85.07	64.59
CC	0.5351	0.7346	0.6586	0.8092

TABLE IV
PIXEL GROUPING RESULT OF EACH PHANTOM

Phantom 1		Phantom 2		Phantom 3		Phantom 4	
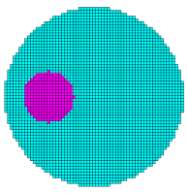	Large group number: 1 Small group number: 2977	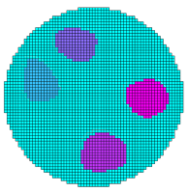	Large group number: 4 Small group number: 2601	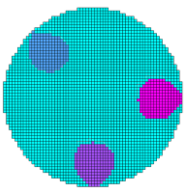	Large group number: 3 Small group number: 2725	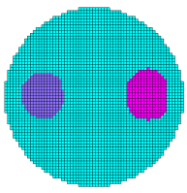	Large group number: 2 Small group number: 2817

Landweber iteration, TV regularization and l_1 regularization, the reconstructed image using AGSP show significantly improved noise reduction performance as well as more accurate position and shape. The result based on AGSP has a much smaller image error, i.e., 47.47%, and higher correlation coefficient, i.e., 0.9192, in comparison with other algorithms. Note that for large objects, the l_1 regularization provides an estimation with too small size. Phantom 2 evaluates multiple small objects with slightly different size and close location. The two spheres located near the bottom are close to each other. The grouping result in TABLE IV indicates that the two spheres near bottom are clustered into a big group due to the low spatial resolution of the conventional algorithm in step 1, TABLE I. However, the group sparsity structure still stands and the

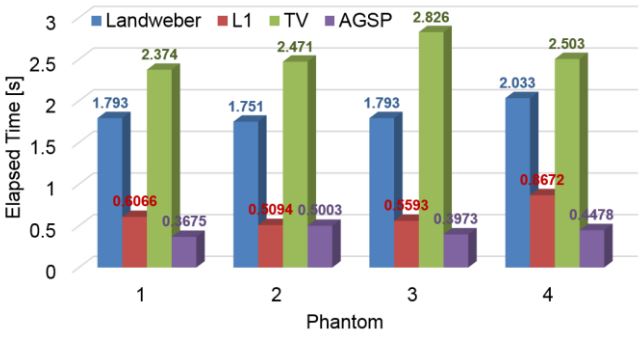

Fig. 5. Comparison of elapsed time of the image reconstruction procedure for each simulation phantom.

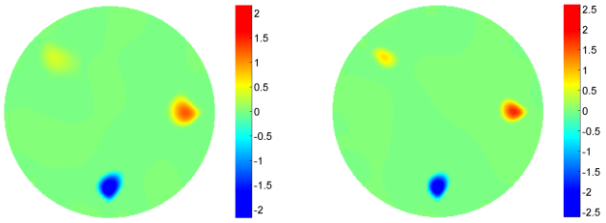

IE: 51.65
CC: 0.8764
(a)

IE: 42.21
CC: 0.9098
(b)

Fig. 6. Comparison of different weight values of AGSP on image quality of Phantom 3. (a) Weight value equals one. (b) Weight calculated based on Eq. (20).

proposed AGSP algorithm is able to further distinguish these two objects after iteration whilst the other algorithms fail to achieve the same performance. Phantom 3 tests objects with three different conductivity values and phantom 4 validates objects with different geometry shapes. For all the test phantoms, the proposed AGSP algorithm demonstrates superior imaging quality with more accurate object shapes, locations, and significantly improved image errors (below 65%) and correlation coefficients (above 0.7621), compared with other given algorithms.

Fig. 5 illustrates the comparison of elapsed time between the Landweber iteration, TV regularization, l_1 regularization and AGSP. The image reconstruction is performed using Matlab 2013a installed on a windows desktop with an Intel Xeon CPU (X5650 @ 2.67 GHz, 2 processors) and 24 GB memory. According to [21], the computation cost each iteration of the ADMM is O(*mn*) when applied to solve Eq. (13). While the computation cost of solving Eq. (7) using the gradient method is O(*nn*). As indicated by Fig. 5, the elapsed time of all phantoms using AGSP is below 0.6 seconds, less than that of other given methods, reassuring a lower computation cost and the feasibility of real-time implementation of AGSP in the future.

Fig. 6 illustrates the effect of weight value of AGSP on image quality, using phantom 3 as an example. Two weighting strategies are considered, i.e., weighting based on Eq. (20) and weighting using all one vector. Fig. 6(b) shows the image using the same weight for all groups. The correlation coefficient and image error of Fig. 6(b) are 0.8764 and 51.65, respectively. It is shown that comparable but slightly lower image quality is obtained if the same weight values are adopted. The result

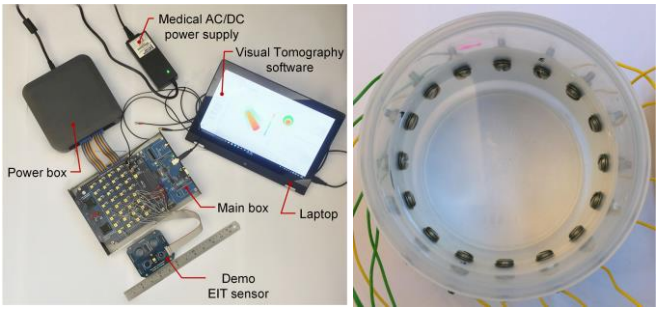

(a) (b)

Fig. 7. The experimental facility. (a) The in-house developed EIT system. (b) The 16-electrode EIT sensor.

validates that by giving a smaller weight to the large group and a larger weight to the small group as formulated by the weighting strategy in Eq. (20), the imaging quality can be further improved as the sparsity of the estimation is promoted.

B. Experiment Results

The performance of AGSP algorithm is further validated by phantom experiments in this subsection. An EIT system for real-time 3D biomedical and industrial imaging is developed in the Agile Tomography Group at the University of Edinburgh. Fig. 7(a) illustrates the picture of the system. The system supports up to 32 electrodes and the working frequency ranges from 10 kHz to 1 MHz. The highest temporal resolution are 1014 frames per second and the highest SNR tested on a saline phantom is 73 dB.

Fig. 7(b) illustrates the 16-electrode EIT sensor used in the experiments. The inner diameter of the sensor is 95 mm. The background substance is saline with a conductivity of 0.05 S · m^{-1} for all test phantoms. In experiments, the current excitation frequency is selected as 10 kHz and the current amplitude is set as 1.5 mA peak to peak. The adjacent sensing strategy is adopted and the amplitude data of the boundary voltage is acquired for image reconstruction.

As illustrated in the first column of TABLE III, four experiment phantoms were imaged, i.e., three glass rods (object-sensor diameter ratio is 6%), a glass rod (object-sensor diameter ratio is 6%) and a metal rod (object-sensor diameter ratio is 7%), three plastic rods (object-sensor diameter ratio is 16%), and three metal rods (object-sensor diameter ratio is 6%). When implementing the algorithms, the maximum iteration of Landweber iteration, l_1 regularization, TV regularization and AGSP algorithm is set to be 500 and the stopping tolerance is set to be 1e-7. Other algorithm parameters are the same with the simulation setup and can be found in the first row of TABLE III. In order to quantitatively evaluate the reconstruction accuracy, the image reconstruction results are normalized to [-1, 1] and relative image error and correlation coefficient depicted in Eq. (21) and Eq. (22) are calculated regarding each phantom. Note that the reconstructed images are only normalized for the calculation of image error and correlation coefficient but not in the displayed images.

TABLE III illustrates the image reconstruction results and corresponding quantitative evaluation based on Landweber iteration, l_1 regularization, TV regularization and the proposed AGSP algorithm. The pixel grouping results and detail group numbers of each phantom are given in TABLE V.

TABLE V
IMAGE RECONSTRUCTION RESULTS BASED ON EXPERIMENT DATA

Phantom	Landweber Step factor α in Eq.(5): 2	L_1 Step factor solving Eq. (6): 2	TV Step factor α in Eq. (11): 2	AGSP d_{max}: 20; **w**: Eq. (20), λ: 0.01
	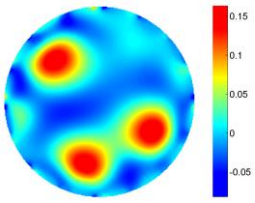	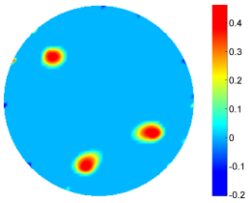	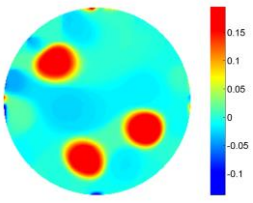	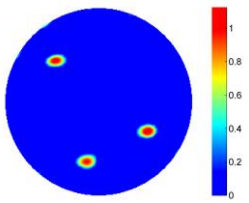
IE [%]	246.4	87.34	240.8	54.04
CC	0.3393	0.6238	0.3328	0.8410
	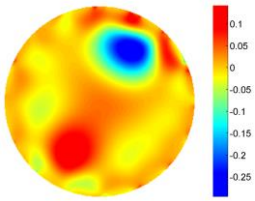	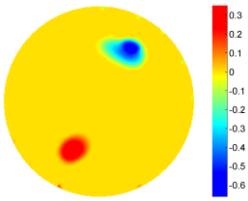	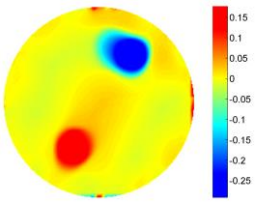	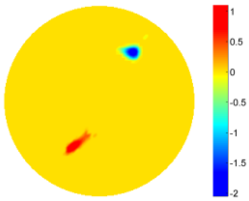
IE [%]	366.8	94.20	335.8	61.53
CC	0.2845	0.5206	0.2788	0.7842
	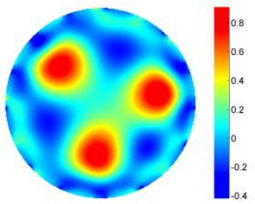	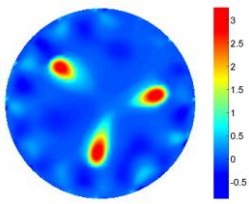	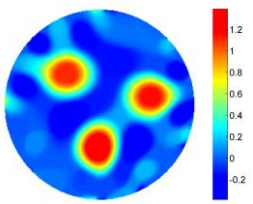	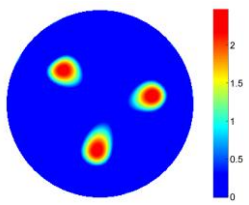
IE [%]	90.44	65.01	71.73	52.41
CC	0.6342	0.7725	0.7251	0.8571
	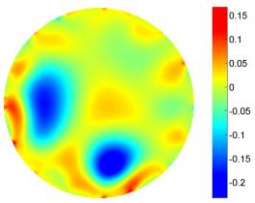	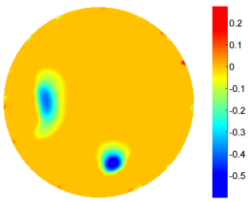	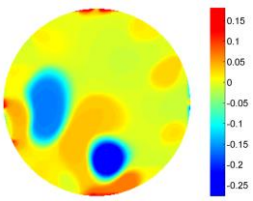	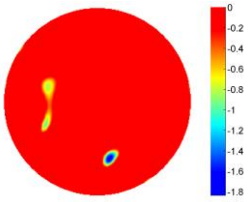
IE [%]	367.3	107.70	267.7	75.40
CC	0.2592	0.4112	0.2454	0.6649

TABLE VI
PIXEL GROUPING RESULT OF EACH PHANTOM

Phantom 1		Phantom 2		Phantom 3		Phantom 4	
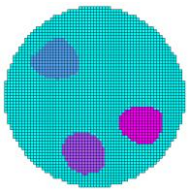	Large group number: 3 Small group number: 2711	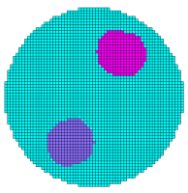	Large group number: 2 Small group number: 2781	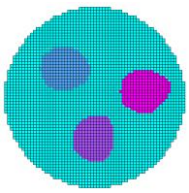	Large group number: 3 Small group number: 2624	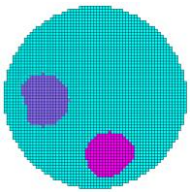	Large group number: 2 Small group number: 2872

Overall, comparable results with simulation are obtained. The proposed AGSP algorithm achieves much smaller image error below 55%, and higher correlation coefficients above 0.84 for the first and the third phantoms, while slightly larger errors for the second and the last phantoms due to the challenging setup. Whilst the compared algorithms, i.e., Landweber iteration, l_1 regularization and TV regularization suffer from much larger image errors and smaller correlation coefficients and cannot distinguish the small objects close to each other. From the results, significant image noise reduction and resolution improvement have been observed by using the AGSP method, indicating much better image quality in comparison with the conventional l_1 and TV algorithms. Additionally, the grouping results demonstrated in TABLE VIII regarding each phantom are reasonable and show similarity with the simulation study.

In summary, the experiment results further confirm the superior performance of the proposed AGSP algorithm under practical setup. The AGSP algorithm can be expected to generate high quality tomographic images especially for the applications requiring enhanced spatial resolution and noise deduction performance, such as cell spheroid imaging in cell culture process sensing and dispersed air bubbles imaging in multiphase flow measurement.

V. Conclusions

In this paper, a novel image reconstruction algorithm using adaptive group sparsity constrained (AGSP) is proposed. The EIT-image-reconstruction problem is modelled with a weighted group-sparse basis pursuit model with nonnegativity constraint. To facilitate fast group structure extraction, an adaptive pixel grouping method is incorporated for dynamic, self-adapting conductivity variation grouping. The proposed AGSP method efficiently utilizes the underlying group sparsity structure as prior knowledge for enhanced imaging performance. Both numerical simulation and static phantom experiments on several challenging conductivity phantoms were carried out for performance evaluation. The results are thoroughly compared with conventional Landweber iteration, l_1 regularization and TV regularization. The results indicate that the proposed AGSP algorithm is able to generate superior tomographic images with higher image quality, better noise deduction performance and improved spatial resolution, in comparison with the other given algorithms.

Future work will study the real-time application of AGSP algorithm and investigate the performance of the proposed algorithm in some challenging applications such as the cell spheroid imaging and real-time monitoring in biomedical research and dispersed bubble identification in multi-phase flow measurement.

Acknowledgment

The work is partly supported by 2015 IEEE Instrumentation & Measurement Society Graduate Fellowship Award.

References

[1] M. Wang et al., "A high-performance EIT system," *IEEE Sens. J.*, vol. 5, no. 2, pp. 289–299, 2005.

[2] L. Miao et al., "ROI-Based Image Reconstruction of Electrical Impedance Tomography Used to Detect Regional Conductivity variation," *IEEE Trans. Instrum. Meas.*, vol. 63, no.12, pp. 2903–2910, 2014.

[3] F. Ricard et al., "Monitoring of multiphase pharmaceutical processes using electrical resistance tomography," *Chem. Eng. Res. Des.*, vol. 83, no. 7, pp. 794–805, 2005.

[4] X. Deng et al., "AC impedance model of array electrodes in multisensor fusion system for two-phase flow measurement," *IEEE Trans. Instrum. Meas.*, vol. 59, no. 6, pp. 1722–1726, 2010.

[5] M. Sharifi et al., "Electrical resistance tomography (ERT) applications to chemical engineering," *Chem. Eng. Res. Des.*, vol. 91, no. 9, pp. 1625–1645, 2013.

[6] R. H. Bayford, "Bioimpedance tomography (electrical impedance tomography)," *Annu. Rev. Biomed. Eng.*, vol. 8, pp. 63–91, 2006.

[7] P. Metherall et al., "Three dimensional electrical impedance tomography," *Nature*, vol. 380, no. 6574, pp. 509–512, 1996.

[8] H. McCann et al., "A portable instrument for high-speed brain function imaging: fEITER," In *Proc. 2011 Annual International Conference of the IEEE Engineering in Medicine and Biology Society*, 2011, pp. 7029–7032.

[9] D. Chen et al., "Design of impedance measuring circuits based on phase-sensitive demodulation technique," *IEEE Trans. Instrum. Meas.*, vol. 60, no. 4, pp. 1276–1282, 2011.

[10] Y. Yang et al., "A novel multi-electrode sensing strategy for electrical capacitance tomography with ultra-low dynamic range," *Flow Meas. Instrum.*, 2016, in press.

[11] H. Wang et al., "An image reconstruction algorithm based on total variation with adaptive mesh refinement for ECT," *Flow Meas. Instrum.*, vol. 18, no. 5, pp. 262–267, 2007.

[12] H. Wang et al., "A pre-iteration method for the inverse problem in electrical impedance tomography. *IEEE Trans. Instrum. Meas.*, vol. 53, no. 4, pp. 1093–1096, 2004.

[13] Y. Yang et al., "Effect of structured packing on EIT image reconstruction," in *Proc. IEEE International Conference on Imaging Systems and Techniques*, 2014, pp. 53–58.

[14] B. Jin et al., "A reconstruction algorithm for electrical impedance tomography based on sparsity regularization," *International Journal for Numerical Methods in Engineering*, vol. 89, no. 3, pp. 337–353, 2012.

[15] J. Ye et al., "Image reconstruction for electrical capacitance tomography based on sparse representation," *IEEE Trans. Instrum. Meas.*, vol. 64, no. 1, pp. 89–102, 2015.

[16] J. L. Mueller et al., "A direct reconstruction algorithm for electrical impedance tomography," *IEEE Trans. Med. Imag.*, vol. 21, no. 6, pp. 555–559, 2002.

[17] Z. Cao et al., "Electrical capacitance tomography with a non-circular sensor using the dbar method," *Meas. Sci. Technol.*, vol. 21, no. 1, p. 015502, 2009.

[18] Z. Cao et al., "2D image reconstruction of a human chest by using Calderon's method and the adjacent current pattern," *Journal of Instrumentation*, vol. 8, no. 03, p. P03004, 2013.

[19] S. J. Hamilton et al., "Direct EIT reconstructions of complex admittivities on a chest-shaped domain in 2-D," *IEEE Trans. Med. Imag.*, vol. 32, no. 4, pp.757–769, 2013.

[20] N. Polydorides et al., "A Matlab toolkit for three-dimensional electrical impedance tomography: a contribution to the Electrical Impedance and Diffuse Optical Reconstruction Software project," *Meas. Sci. Technol.*, vol. 13, no. 12, p. 1871, 2002.

[21] W. Q. Yang et al., "Image reconstruction algorithms for electrical capacitance tomography," *Meas. Sci. Technol.*, vol. 14, no. 1, R1, 2002.

[22] W. R. B. Lionheart, "EIT reconstruction algorithms: pitfalls, challenges and recent developments," *Physiol. Meas.*, vol. 25, no. 1, p. 125, 2004.

[23] E. J. Candès et al., "An introduction to compressive sampling," *IEEE Signal Processing Magazine*, vol. 25, no. 2, pp. 21–30, 2008.

[24] J. Huang et al., "The benefit of group sparsity," *The Annals of Statistics*, vol. 38, no. 4, pp. 1978–2004, 2010.

[25] F. Dong et al., "Two methods for measurement of gas-liquid flows in vertical upward pipe using dual-plane ERT system," *IEEE Trans. Instrum. Meas.*, vol. 55, no. 5, pp. 1576–1586, 2006.

[26] Y. Yang et al., "A Miniature Electrical Impedance Tomography Sensor and 3-D Image Reconstruction for Cell Imaging," *IEEE Sens. J.*, vol. 17, no. 2, pp. 514–523, 2017.

[27] W. Q. Yang et al., "An image reconstruction algorithm based on Landweber's iteration method for electrical capacitance tomography," *Meas. Sci. Technol.*, vol. 10, pp. 1065–9, 1999.

[28] V. D. B. Ewout et al., "Probing the Pareto frontier for basis pursuit solutions," *SIAM Journal on Scientific Computing*, vol. 31, no. 2, pp. 890–912, 2008.

[29] S. Osher et al., "An iterative regularization method for total variation-based image restoration," *Multiscale Modeling & Simulation*, vol. 4, no. 2, pp. 460–464, 2005.

[30] A. Beck et al., "Fast gradient-based algorithms for constrained total variation image denoising and deblurring problems," *IEEE Transactions on Image Processing*, vol. 18, no. 11, pp. 2419–2434, 2009.

[31] Y. Yang et al., "Data pattern with ECT sensor and its impact on image reconstruction," *IEEE Sens. J.*, vol. 13, no. 5, pp. 1582–1593, 2013.

[32] M. Fukushima et al., "Application of the alternating direction method of multipliers to separable convex programming problems," *Computational Optimization and Applications*, vol. 1, no. 1, pp. 93–111, 1992.

[33] W. Deng et al., "Group sparse optimization by alternating direction method," In *SPIE Optical Engineering+ Applications*, pp. 88580R–88580R, 2013.
[34] B. H. Brown et al., "The Sheffield data collection system," *Clinical Physics and Physiological Measurement*, vol. 8, no. 4A, p. 91, 1987.

Yunjie Yang (M'13) received the B.Eng.(hons) and M.Sc.(hons) degrees in measurement & control engineering at Anhui University, China, in 2010, and Tsinghua University, China, in 2013, respectively. Currently he is a PhD candidate with the Agile Tomography Group, School of Engineering, University of Edinburgh, UK. His current research interest includes Electrical Impedance Tomography and Electrical Capacitance Tomography for biomedical and industrial imaging. He is the recipient of 2015 IEEE I&M Society Graduate Fellowship Award.

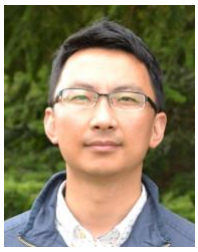

Jiabin Jia (M'15) was born in Inner Mongolia, China, in 1980. He received the B.Eng. and Master degree in Electrical and Electronics Engineering from the Wuhan University, China, in 2002 and 2005 respectively. After working for one year in H3C Technology Co., Ltd as a hardware engineer, he started his PhD study at the University of Leeds supported by the Overseas Research Students Award Scheme Award in 2006 and completed in 2010. Then he was a Research Fellow and worked on an EPSRC project for three years. In October 2013, he was appointed as a Lecturer in the School of Engineering, the University of Edinburg. His current research interests include electrical tomography, multiphase flow measurement, instruement development and medical imaging.